

Kink instability of flux ropes anchored at one end and free at the other

Giovanni Lapenta,^{1,2} Ivo Furno,³ Thomas Intrator,² and Gian Luca Delzanno²

Received 20 June 2006; revised 22 September 2006; accepted 3 October 2006; published 16 December 2006.

[1] The kink instability of a magnetized plasma column (flux rope) is a fundamental process observed in laboratory and in natural plasmas. Previous theoretical, experimental, and observational work has focused either on the case of periodic (infinite) ropes (relevant to toroidal systems) or on finite ropes with both ends tied to a specified boundary (relevant to coronal ropes tied at the photosphere). However, in the Sun's corona and in astrophysical systems there is an abundant presence of finite flux ropes tied at one end but free at the other. Motivated by recent experiments conducted on the RSX device (Furno et al., 2006) and by recent theoretical work (Ryutov et al., 2006), the present paper investigates by simulation the linear and nonlinear evolution of free-ended flux ropes. The approach is based on comparing the classic case of a periodic flux rope with the case of a rope tied at one end and free at the other. In the linear phase, periodic and free ropes behave radically differently. A simulation analysis of the linear phase confirms the experimental and phenomenological findings relative to an increased instability of a free rope: the new stability limit is shown to be just half of the classic limit for periodic ropes. In the nonlinear phase, reconnection is observed to be a fundamental enabler to reach the eventual steady state. The mechanism for saturation of a flux rope is investigated and compared with the classic theory (the so-called bubble state model) by Rosenbluth et al. (1976). A remarkable agreement is found for the classic periodic case. The case of a free rope is again very different. The saturated state is observed to present a outwardly spiraling configuration with the displacement of the plasma column increasing progressively and monotonically from the tied end to the free end. The maximum displacement is observed at the free end where it is consistent with the displacement observed in a periodic rope. The key distinction is that in a periodic rope the same displacement is observed throughout the whole rope to form a helix with constant radius.

Citation: Lapenta, G., I. Furno, T. Intrator, and G. L. Delzanno (2006), Kink instability of flux ropes anchored at one end and free at the other, *J. Geophys. Res.*, *111*, A12S06, doi:10.1029/2006JA011932.

1. Introduction

[2] The kink instability is a classic problem in plasma physics. It is a crucial consideration in the stability of fusion devices [Wesson, 2004] and it is a common occurrence in space and solar physics. For example, flux ropes observed in the solar corona and in the magnetosphere can be unstable to the kink mode and such instability has been observed and studied widely in the literature [Priest and Forbes, 2000]. Figure 1 shows an examples of a solar corona image where multiple flux tubes are observed. Movies are available of satellite observations showing the dynamic behavior of such coronal loops.

[3] Similarly, astrophysical observations show the presence of magnetized jets emitted from accreting objects. For example, Figure 2 shows one of such jets emitted from the galaxy M87, observed here in the radio frequency range at VLA.

[4] The kink instability has been studied extensively in previous literature. Section 4 reviews the previous work of interest to the present study, but the kink mode is a classic textbook plasma physics instability [see, e.g., Goedbloed and Poedts, 2004]. The vast majority of the previous work referred to the case of a periodic rope as appropriate for a toroidal plasma where a plasma column closes on itself.

[5] In the solar physics community, flux ropes tied to the solar corona have been also considered [see, e.g., Hood and Priest, 1979]. In that case the photosphere is assumed to be so much heavier to hold fixed the ends of flux ropes linked to it. However, as can be observed in Figure 1, some flux ropes become detached from the photosphere at one end (see upper left corner of Figure 1). This situation is common in coronal holes where the field lines are open and one end extends into the solar system. However, free-

¹Centre for Plasma Astrophysics, Departement Wiskunde, Katholieke Universiteit Leuven, Heverlee, Belgium.

²Los Alamos National Laboratory, Los Alamos, New Mexico, USA.

³Ecole Polytechnique Federale de Lausanne (EPFL), Centre de Recherches en Physique des Plasmas, Association EURATOM-Confederation Suisse, Lausanne, Switzerland.

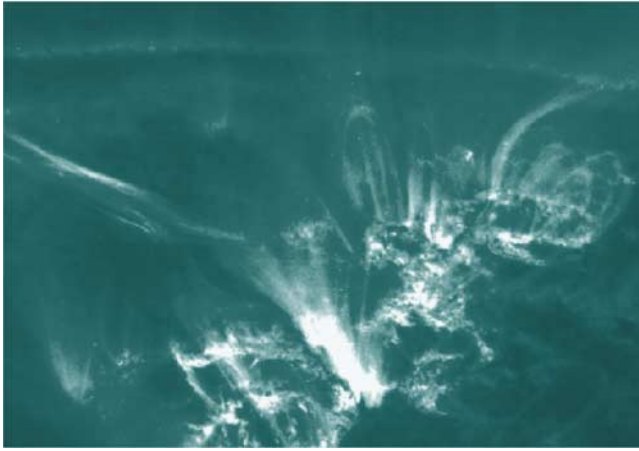


Figure 1. Image of Active Region 9373 (rotated counter-clockwise over 90 degrees), taken by TRACE [Schrijver *et al.*, 1999] in its 171 Å pass band on 2001-3-21.

ended ropes may become in existence even in regions of normally closed field lines, during the dynamical evolution of the corona where reconnection can lead to the breakup of field lines that get detached from the corona at one end, thereby releasing energy from the corona outward into the solar system. Such processes are for example part of the mechanisms believed to be behind the so-called coronal mass ejections [Priest and Forbes, 2000].

[6] Similarly, in the case of astrophysical jets, the tying of the rope is working at one end only, at the end attached to the object creating the jet [Blandford, 2002], but the other end of the jet is clearly free. In the example in Figure 2 the jet is believed to be created in an accretion disk around a black hole present in the center of galaxy M87 (an elliptical galaxy also known as NGC 4486 and Virgo A).

[7] The primary novelty of the present paper is in investigating with nonlinear numerical simulations the kink instability for free ended systems. Our analysis reaches two main conclusions.

[8] First, we confirm the predictions of a previous phenomenological linear theory [Ryutov *et al.*, 2006] via numerical simulations. Our numerical simulations show that indeed a system where the field lines are tied at one end but free at the other is more unstable than the corresponding periodic (or toroidal) system. This latter configuration is in itself more unstable than a system line-tied at both ends, making the free-ended system more unstable than all systems previously considered. Periodic systems are unstable when the current exceeds the Kruskal-Shafranov (KS) limit [Goedbloed and Poedts, 2004], corresponding to the situation when a surface exists inside the plasma where the safety factor $q = 1$. In the system line-tied at one end and free at the other, the kink instability appears as soon as $q < 2$ within the plasma. Note that a rope line-tied at both ends is more stable than a periodic rope only when a conducting wall is close enough to the rope. In the case of a far conducting wall, the instability threshold is the same for both cases [Ryutov *et al.*, 2004].

[9] Second, we investigate the saturation mechanism for the instability. We observe that the instability grows on a Alfvénic timescale until the plasma region reaches the mode resonant surface. The evolution afterwards require the process of reconnection. Eventually, the flux rope reaches saturation at a surface that can be well predicted using the so-called bubble-state model introduced by Rosenbluth *et al.* [1976] for periodic systems. A free-ended rope evolves through the same stages as a periodic rope, but its saturation state shows an outward spiraling where the outer radius of the rope is progressively displaced, from zero displacement at the tied end to a maximum displacement at the free end. The maximum displacement of the free end is still consistent with the model by Rosenbluth *et al.* [1976].

[10] The paper is organized as follows. Section 2 describes the specific setting used in the present paper to describe the evolution of flux ropes. The configuration considered is specific to the RSX device [Furno *et al.*, 2003] where flux ropes can be studied directly experimentally. Section 3 describes the simulation method used to study the evolution.

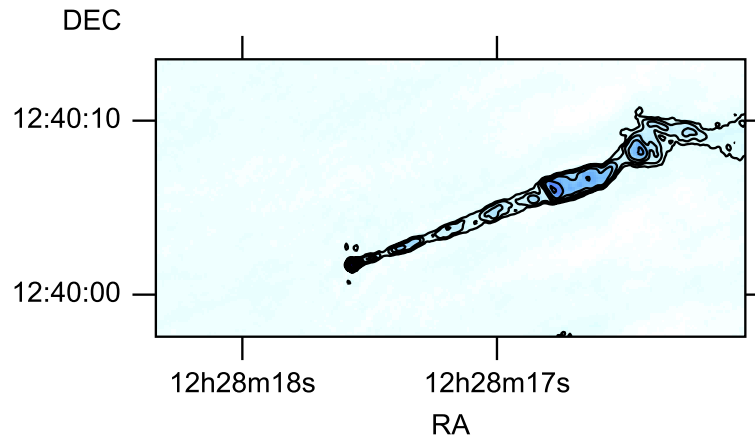


Figure 2. Jet ejected from galaxy M87. Radio intensity at 14.435 GHz observed at VLA on 1994-5-2 [Owen *et al.*, 1989]. On the left side, a flux rope tied at one end and free at the other is shown to form during the course of an eruption.

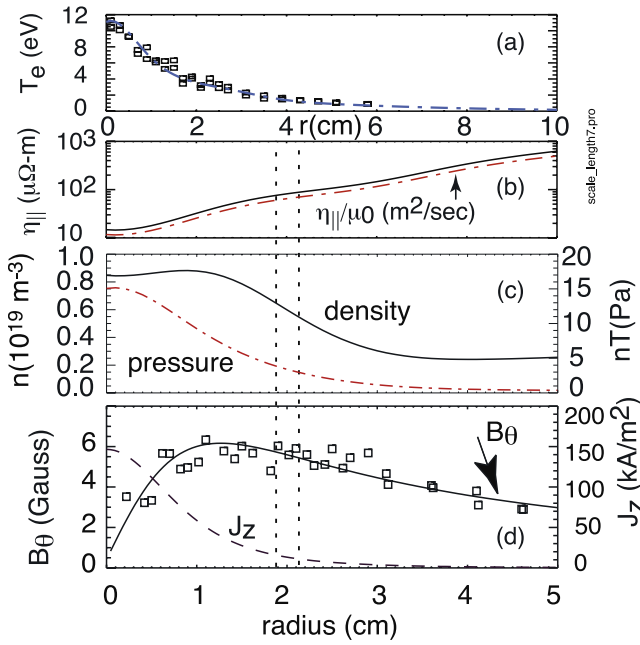


Figure 3. Experimental data from a typical plasma shot. From top to bottom profiles of the plasma properties are shown: (a) electron temperature, (b) parallel resistivity, (c) density and pressure, and (d) tangential magnetic field and current. SI units are used.

[11] Section 4 focuses on the linear stability comparing previous predictions and experimental observations at RSX with numerical simulations. The conclusion, as noted above, is that the most unstable case is that of flux ropes with one free end, followed by periodic ropes. Line-tied flux ropes, instead, are shown to be more stable than both.

[12] Nonlinear evolution and saturation are described in sections 5 and 6. Section 5 focuses on the reference case of a periodic rope where previous theories can be validated. Section 6 deals with the case of a rope free at one end and tied at the other. Comparison between the two cases is made. A qualitative agreement with experimental observation is also provided. Conclusions are drawn in section 7.

2. Description of the System Under Consideration

[13] The Reconnection Scaling Experiment (RSX) at Los Alamos National Laboratory is described by Furno *et al.* [2003, 2005] and takes advantage of recently developed plasma gun technology [Fiksel *et al.*, 1996] to create a flux rope that is initially linear but supports fully three-dimensional (3-D) evolution. One key attribute of RSX is the ability to continuously adjust the axial guide field ($B_{0z} = 0\text{--}2$ kGauss) and ion gyro radius independently of the plasma and current density, providing scans of plasma β . RSX is one of a few devices [Hansen *et al.*, 2004; Gekelman *et al.*, 1992] that have ever been used to study flux 3-D rope dynamics.

[14] Typical plasma parameters are density $n_e \approx 3 \times 10^{13} \text{ cm}^{-3}$, electron temperature $T_e \approx 3\text{--}12 \text{ eV}$, $B_{0z} = 100 \text{ G}$, $B_\theta \leq 10 \text{ G}$, $\beta \approx 0.5$. Typical current rope radius is 2.5 cm. The Alfvén time is of few μs , while the resistive diffusion time is of the order of 100 μs . For the experimental data

shown here, the flux rope current I_{rope} ramps up with a selected e-folding time, and instability grows and saturates for $100 \text{ A} < I_{\text{rope}} < 400 \text{ A}$. Figure 3 shows the typical profiles observed in RSX.

[15] The RSX has a cylindrical vacuum chamber (4 m length \times 0.2 m radius) much larger than the flux rope dimension (0.5–1.5 m length \times 0.03 m radius). For the experiments relevant to the present work, one plasma gun [Fiksel *et al.*, 1996] was radially inserted from the top as shown in Figure 4. The plasma gun contains a miniaturized plasma source with a circular 0.4 cm radius nozzle aperture in which a hydrogen plasma is produced by an arc discharge. The arc plasma is maintained for ≈ 10 ms by a pulse forming network from which a current is drawn during a ≈ 1.5 ms pulse that biases the external anode positive relative the floating gun arc. The external anode location along the z axis determines the flux rope length. The constant, uniform, axial (in the z direction) background magnetic field B_{0z} , can be varied within the range 0–2 kGauss.

[16] To describe the plasma in RSX, we rely on a simple model that captures qualitatively the main features of the plasma generated in RSX but thanks to its simplicity and generality can be easily related to configurations relevant to space and astrophysical systems. We consider a simple mathematical model of a flux rope based on the textbook screw pinch [Freidberg, 1987]. The magnetic field expression in cylindrical (r, θ, z) coordinates is

$$\begin{aligned} B_\theta &= \frac{B_0 r}{r^2 + w^2} \\ B_z &= 1 \\ B_r &= 0 \end{aligned} \quad (1)$$

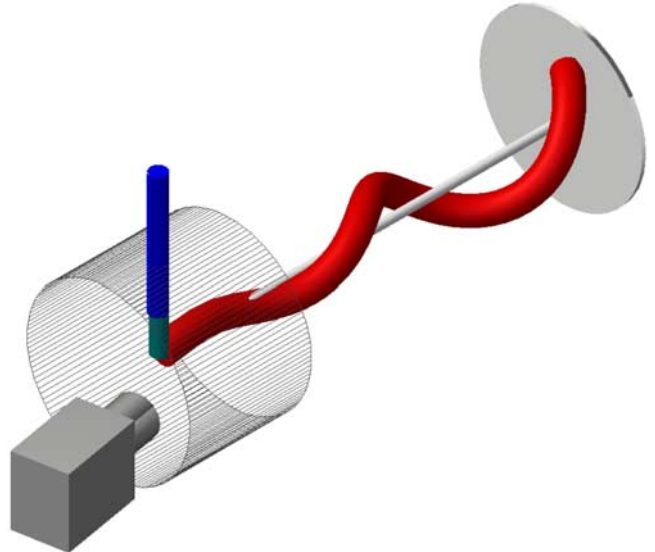


Figure 4. Artist's rendition of the experimental configuration simulated in the present paper. One plasma gun produces a flux rope in a cylindrical vessel with an axial magnetic field generated by outside coils. The rope generates its own tangential field and can be unstable to the kink instability, as shown. The position and view angle of the camera are shown.

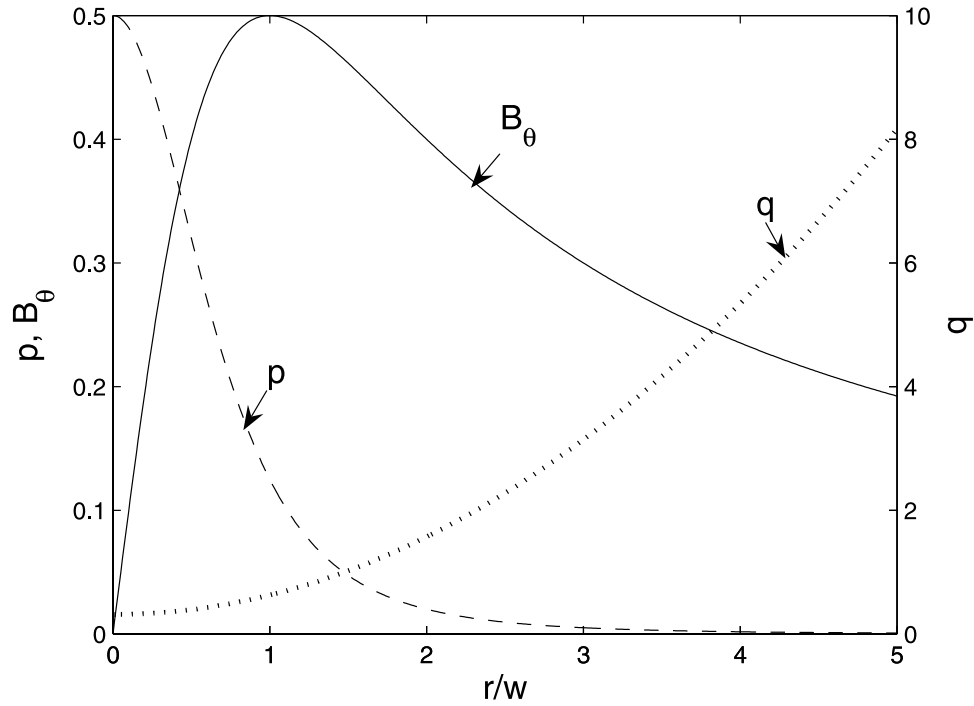


Figure 5. Initial magnetic field B_θ (solid), pressure (dashed) and safety factor q (dash-dotted) profile for a case with $B_0 = 1$.

representing an helical magnetic field with helical pitch determined by the amplitude of the θ component (i.e., by B_0).

[17] The magnetic field is not force free and is in balance with a plasma pressure:

$$p = \frac{B_0^2 w^2}{2\mu_0(r^2 + w^2)^2} \quad (2)$$

Since the pressure is equal to $p = \rho kT$, the freedom in the relative choice of the density and temperature is used to best represent the plasma in RSX, where the temperature and density have a similar profile: $\rho = kT = \sqrt{p}$. In some reference runs below a uniform density ρ_0 is also considered.

[18] Figure 5 shows the initial pressure and poloidal magnetic field profile for the case $B_0 = 1$. The surface $q = 1$ is completely external to the bulk of the plasma resulting in a configuration suitable to study external kink modes. The configuration described above represents a reasonable qualitative model of a flux rope in RSX. The approximate scale is determined by comparing the wall radius and the temperature profile (directly linked to the Spitzer resistivity): one unit of the simulations corresponds to 4 cm in the real device. Below, we study the stability properties of such a flux rope in conditions valid and applicable to all the cases just listed.

3. Simulation Approach

[19] All simulations are carried out using the FLIP3D-MHD code [Brackbill, 1991] based on the standard

viscoresistive MHD model. The viscoresistive MHD model, written in the Lagrangian frame, is summarized by mass continuity,

$$\frac{d\rho}{dt} = -\rho \nabla \cdot \mathbf{v}, \quad (3)$$

Faraday's law,

$$\frac{d}{dt} \left[\frac{\mathbf{B}}{\rho} \right] = \frac{\mathbf{B}}{\rho} \cdot \nabla \mathbf{v} - \frac{1}{\rho} [\nabla \times \eta \mathbf{J}], \quad (4)$$

where a resistive Ohm's law is assumed,

$$\mathbf{E} = \eta \mathbf{J} - \mathbf{v} \times \mathbf{B}, \quad (5)$$

momentum conservation,

$$\rho \frac{d\mathbf{v}}{dt} = -\nabla \left[p + r + \frac{\mathbf{B}^2}{2} \right] + \nabla \cdot \mathbf{B} \mathbf{B}, \quad (6)$$

internal energy equation

$$\rho \frac{dI}{dt} = -p \nabla \cdot \mathbf{v} + \eta (\mathbf{J} \cdot \mathbf{J}). \quad (7)$$

and by Ampere's law,

$$\nabla \times \mathbf{B} = \mu_0 \mathbf{J} \quad (8)$$

[20] The flow variables are the mass density, ρ , the magnetic field, \mathbf{B} , the current density, \mathbf{J} , the fluid velocity, \mathbf{v} ,

the specific internal energy, I , and the plasma pressure p . Here μ_0 is the magnetic permeability, η is the resistivity. The pressure is given by an ideal gas equation of state, $p = (\gamma - 1)\rho I$. The viscous term, r , is given by the Navier-Stokes formula [Brackbill, 1991], where ν is the scalar viscosity.

[21] The resistivity is chosen either uniform ($\eta = \eta_0$) or according to Spitzer's resistivity law [Spitzer, 1956]:

$$\eta = \eta_0 T^{-3/2} \quad (9)$$

where the temperature is defined as usual: $T = p/kn$. Note that the Spitzer resistivity model typically provides an insufficient description of the actual resistivity in space and astrophysical plasmas, and even in fusion experimental devices, where anomalous effects dominate. However, in many lower temperature experimental devices (including RSX), the Spitzer resistivity model provides a reasonable first-order model of the relatively collisional plasma present [Trintchouk et al., 2003; Furno et al., 2005]. To express the reference resistivity, we use the Lundquist number defined as $S = v_A w / \eta_0$, and to express the uniform viscosity, we use the Reynolds number defined as $Re = v_s w / \nu$, where v_s is the sound speed.

[22] FLIP3D-MHD is based on the fluid particle in cell (PIC) method [Brackbill, 1991] that uses particles to model the fluid advection but uses a computational grid to solve the evolution equations for the fluid quantities written in Lagrangian form. The time discretization is implicit to allow larger time steps [Brackbill, 1991]. The approach in FLIP3D-MHD is distinct from the SPH method [Monaghan, 1992] that uses particles and interaction kernels also to solve for the fluid quantities. Also, it is distinct also from grid-based methods that discretize the advection term on the grid as well. The condition $\nabla \cdot \mathbf{B} = 0$ is imposed at each time step. Space is scaled to the characteristic length of the initial equilibrium w , density is normalized to the uniform reference value ρ_0 and time is scaled by the Alfvén time, $\tau = L/v_A$, where v_A is the Alfvén speed. The magnetic permeability μ_0 is unitary.

[23] FLIP3D-MHD has been previously used and applied in a number of studies [Brackbill and Knoll, 2001; Lapenta and Knoll, 2004, 2005; Lapenta and Kronberg, 2005]. The coordinate system chosen in the code is cartesian. This differs significantly from the typical plasma physics code that uses cylindrical coordinates. Here the system is represented by a parallelepipedal domain of size $L_x = L_y = 10w$ and $L_z = 20w$. The actual circular wall of the device is described with the immersed boundary method.

[24] The immersed boundary method [Peskin, 2002] allows the description of arbitrarily (and even changing) boundaries or interfaces between materials. The method is extremely powerful, especially when combined with non-uniform or adaptive grids and has been applied successfully to numerous applications [Peskin, 2002]. However, the case at hand is very simple and the immersed boundary method becomes straightforward. The interface is a circle embedded in a uniform cartesian grid. The metal vessel of RSX is represented by assigning material particles everywhere outside a circle corresponding to radius $R = 5w$. The plasma inside the vessel is then represented by regular computational particles that represent Lagrangian markers evolving

according to the MHD equations. The computational particles outside the circle are stationary and represent a material with zero resistivity (for an ideal wall, easily generalizable to resistive walls).

[25] The immersed boundary method correctly represents the response of a metal wall: it imposes no radial plasma velocity at the wall and it imposes the correct boundary conditions on the magnetic field. The use of the immersed boundary method in a PIC description of fluid equations of any type results in an effective replacement of a sharp boundary with a diffuse transition with a thickness equivalent to the size of the computational particle [Lapenta and Brackbill, 1996; Lapenta et al., 1995]. In FLIP3D-MHD the particle size is chosen to be in each direction equal to the corresponding grid spacing. The interfaces become transition regions of thickness equal to the cell size. The effect of the finite transition introduces a discretization error of the same order as the error already introduced by discretizing the operators. Except for special circumstances, there is no reason for imposing exact boundary conditions to operators discretized with a certain truncation error. However, it is crucial that the discretization error be kept of the same order as the truncation error on the interior domain to prevent the solution from being dominated by boundary errors. We have used the approach in previous publications [Lapenta and Brackbill, 1996; Lapenta et al., 1995; Lapenta, 1999, 2002] and we have further tested the approach here recovering the vacuum field solution within the expected truncation error and we have verified a posteriori that the boundary conditions are indeed correctly imposed on the boundary.

[26] The boundary conditions at the end walls ($z = 0$ and $z = L_z$) are chosen in three different ways to represent different experimental or natural situations. First, periodic boundary conditions are applied to represent conditions typical of toroidal devices or closed ropes. In this case the actual toroidal rope is represented as a straight periodic cylinder.

[27] Second, to represent conditions believed to be typical of solar coronal plasmas line tying is applied at both ends of the flux rope. For such a case the velocity field is chosen to be zero at both ends by applying Dirichlet boundary conditions.

[28] Finally, in some parts of the solar corona, e.g., in the coronal holes and in some active regions (see Figure 1) of the corona, flux ropes are present anchored at one end on the solar surface but free at the other. The same configuration is prevalent in astrophysical jets (see Figure 2). As noted above, the flux ropes produced in RSX are anchored at the plasma gun but different conditions can be chosen at the other end, ranging from nearly free motion to line tying, depending on the choice of the end electrode.

[29] For the free boundary condition, we follow the prevalent choice in the literature, i.e., the application of Neumann boundary conditions [Zwingmann, 1987]:

$$\left. \frac{\partial \mathbf{v}}{\partial z} \right|_{z=L_z} = 0 \quad (10)$$

often used in solar and astrophysical simulation to represent an open boundary. Similar expressions hold for all other fields.

[30] For RSX this is a reasonable approximation of the plasma behavior at the end cathode where a sheath forms. Previous studies of such sheath [Ryutov *et al.*, 2006] shows that the correct condition to apply is

$$\left. \frac{\partial \mathbf{v}}{\partial z} \right|_{z=L_z} = \kappa \mathbf{v} \quad (11)$$

The two conditions above are extreme cases of this condition, Dirichlet conditions corresponding to $\kappa \rightarrow \infty$ and Neumann conditions corresponding to $\kappa = 0$. Intermediate values of κ would result in intermediate results between the two cases considered here.

[31] In the results below the simulation box has dimensions $[-L_x, L_x]$, $[-L_y, L_y]$ and $[0, L_z]$ with $L_x = L_y = 5$ and $L_z = 20$. The system is discretized using a regular grid of $75 \times 75 \times 150$ Lagrangian markers (particles), with 27 particles per cell in a $25 \times 25 \times 50$ grid with a time step $\Delta t/\tau_A = 0.1$.

4. Stability of the Kink Mode

[32] The initial configuration described in section 2 is liable to become unstable to the kink instability [Kadomtsev, 1992; Wesson, 2004; White, 2001]. The stability of a plasma with arbitrary shape needs to be computed numerically [Wesson, 2004], but for simple configurations with flat current profiles surrounded by vacuum and by ideal walls can be computed analytically [Goedbloed and Poedts, 2004; Kadomtsev, 1992; White, 2001]. Previous results have indicated that the stability of kink modes depends strongly on the applied boundary conditions.

[33] The system under investigation is surrounded in the radial direction by a circular metal wall that could provide stabilization. This configuration is clearly suitable to the experiment RSX but it introduces a significant deviation from the reality of space and astrophysical systems. The effect of the surrounding walls, including their finite resistivity, is one of the most active areas of research in fusion plasmas [Wesson, 2004] and will not be addressed here.

[34] In the present work the attention is focused on the effects of the boundary conditions imposed in the axial direction. The axial conditions are directly linked with the mechanisms creating and sustaining a flux rope. As noted above, we consider periodic, open, and line tying conditions suitable for different natural and manmade plasmas. Below, the previously published conclusions are summarized limiting the scope to the previous results of interest to the present discussion.

[35] Most of the analysis of kink modes has been focused on the application to toroidal plasmas where periodic boundary conditions are appropriate in the straight-cylinder approximation. In this case a flux rope becomes unstable to the kink mode when the current exceed the so-called Kruskal-Shafranov (KS) limit [Goedbloed and Poedts, 2004]:

$$I_{KS} = \frac{(2\pi a)^2 B_z}{\mu_0 L} \quad (12)$$

where L is the length of the rope, a is its radius, and B_z is the axial magnetic field, assumed uniform. Although, the KS

limit is most easily derived for uniform current profiles, its validity is more general [Goedbloed and Poedts, 2004].

[36] An alternative formulation of the KS limit, very popular in the fusion literature, is based on introducing the so-called safety factor:

$$q(r) = \frac{2\pi r B_z}{B_\theta(r) L} \quad (13)$$

that has the geometrical meaning of inverse of the pitch angle of the magnetic field lines, with $q = 1$ meaning that the field lines close upon themselves after one turn (in a periodic rope) [Goedbloed and Poedts, 2004]. The stability limit of the kink mode can be easily formulated in terms of the safety factor by the statement that $q > 1$ everywhere in the domain for the plasma to be stable.

[37] Previous work has shown that when the axial boundary conditions are changed the stability of a flux rope to the kink mode is modified. As can be imagined, flux ropes free at one end are more unstable, while flux ropes tied at both ends are more stable.

[38] Line tying at both ends of a flux rope has been addressed primarily in the solar physics community. The main conclusion of relevance here is twofold. First, line tying increases the stability of a flux rope by increasing the limit current beyond the KS limit [Hood and Priest, 1981; Einaudi and Van Hoven, 1983; Ryutov *et al.*, 2004; Evstatiev *et al.*, 2006]. The eigenfunctions are no longer harmonic functions (with displacement forced to remain zero at the line-tied ends). Second, the nonlinear saturation level is reduced because the flux ropes remain anchored and cannot move in the region close to the ends [Baty *et al.*, 1998; Lionello *et al.*, 1998b], changing the nonlinear evolution and leading to localized current sheet formation [Lionello *et al.*, 1998a].

[39] In the present paper the periodic and line-tied cases are primarily used as comparison for the case of a flux rope line-tied at one end and free at the other. As noted above, this situation is typical of jets in astrophysical systems and for open field lines in the solar corona, anchored on the photosphere at one end only.

[40] The case of open boundary conditions has been considered in a previous work directed specifically at the conditions prevalent in RSX [Ryutov *et al.*, 2006; Furno *et al.*, 2006]. In that case the end electrode forms a sheath where the flux rope is nearly free to roam. A linear theory based on a model of the sheath leads to the conclusion that flux ropes tied at one end and free at the other are more unstable than periodic or line-tied ropes. Indeed, it was shown that the current for the instability limit drops to just half of the KS limit. In terms of the safety factor, a free-ended rope is stable if $q > 2$ everywhere in the domain. We note that in the previous work by Ryutov *et al.* [2006] the boundary conditions represent the sheath in RSX, while here the focus is on Neumann boundary conditions to represent a completely free-ended flux rope.

[41] The increased susceptibility to the kink instability of a rope free at one end and tied at the other is not a foregone conclusion. The tying tends to stabilize the rope and the open boundary condition allows the release of energy at the open boundary, possibly reducing the availability of free energy for the instability. Yet, previous theoretical work [Ryutov *et al.*, 2006] has proposed that a reduced KS limit

Table 1. Benchmark of the Linear Growth of the Kink Instability in a Periodic Plasma Column^a

m	n	Linear Theory $\gamma\tau_A$	Simulation $\gamma\tau_A$
$m = 1$	$n = 1$	0.080	0.05 ± 0.02
$m = 1$	$n = 2$	0.121	0.13 ± 0.02
$m = 1$	$n = 3$	0.029	0.04 ± 0.02
$m = 2$	$n = 2$	0.0017	0.03 ± 0.02
$m = 2$	$n = 3$	0.0326	0.04 ± 0.02
$m = 2$	$n = 4$	0.0787	0.06 ± 0.02
$m = 2$	$n = 5$	0.0730	0.05 ± 0.02
$m = 2$	$n = 6$	0.0119	0.02 ± 0.02

^aThree unstable $m = 1$ modes are present with different axial numbers $n = 1, 2, 3$ and five with $m = 2$ and $n = 2, 3, 4, 5, 6$.

applies and recently, experimental evidence has confirmed this suggestion [Furno *et al.*, 2006]. Below, the effect on the kink instability of allowing one free end in a flux rope is investigated by simulation.

4.1. Periodic (Infinite) Flux Ropes

[42] The periodic case is repeated here for reference and to provide a validation of the simulation code used here. A system with $B_0 = 1$, uniform density and uniform resistivity (corresponding to $S = 10^3$) is considered. The radial dependence of the safety factor is shown in Figure 5.

[43] The minimum value of q occurs in the center and is $q = \pi/10$, corresponding to a severely unstable periodic configuration. Table 1 reports the unstable $m = 1$ and $m = 2$ modes computed with a stability linear code and from a simulation conducted using the FLIP3D-MHD code with the approach described above (section 3). The modes are defined by a Fourier series analysis where the quantum number m refers to the θ angular (poloidal) direction and n to the axial (toroidal) direction.

[44] The results of the linear theory are obtained by an independent stability code. Some details of the implementation of the reference linear code used here are described by Evstatiev *et al.* [2006]. In summary the equations of viscoresistive MHD, equations (3)–(8), are linearized with respect to a given equilibrium and the temporal and θ, z dependence of the unknowns is assumed of the form $\exp[i(\omega t + m\theta + 2\pi n z/L_z)]$ (where m and n are the poloidal and axial wave number, respectively, and ω is the frequency of the perturbation). The equations, which are now only dependent upon radius, are then discretized with finite difference techniques on a uniform computational grid in the radial direction, for fixed m and n . The problem is finally cast as an eigenvalue problem for ω and standard root-finding techniques are used to compute the stability of the system. The results presented here have been obtained with $N_r = 5000$ discretization points which are enough to insure the convergence of the eigenvalue on the third digit.

[45] The simulation is conducted without any initial perturbation and a multitude of modes is excited by the initial discretization error. Figure 6 shows the results of the Fourier analysis of the tangential component of the velocity field (\mathbf{v}_θ) for the $m = \pm 1, n = 1, 2, 3$ modes. The $m = 1$ and $m = -1$ modes are excited to a different degree, depending on the initial perturbation provided by the use of a cartesian grid to represent a cylindrically symmetric state. Such perturbation is uncontrolled but can be reduced by refining

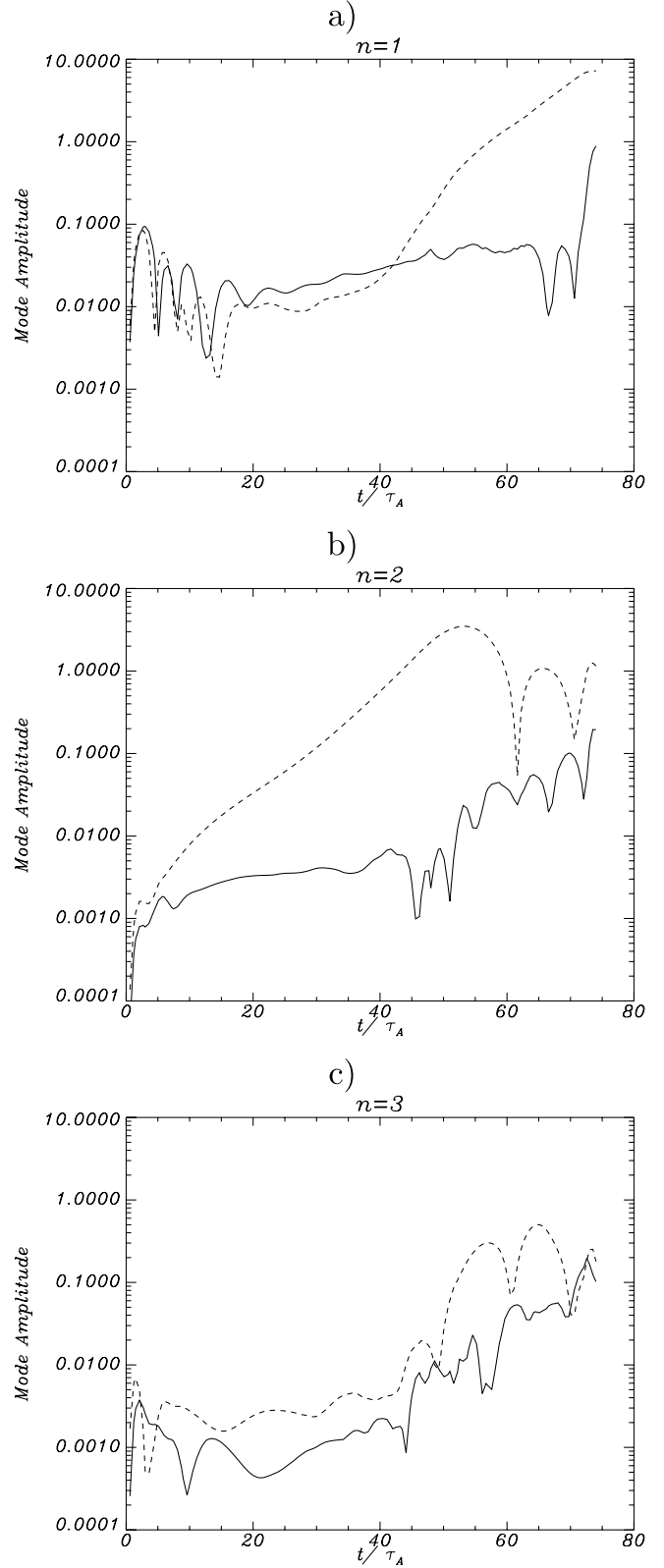


Figure 6. Evolution of the amplitude of the three unstable $m = 1$ (solid) and $m = -1$ (dashed) modes in a periodic system. Run with uniform viscosity (Reynolds number $Re = 10^3$) and resistivity (Lundquist number $S = 10^3$).

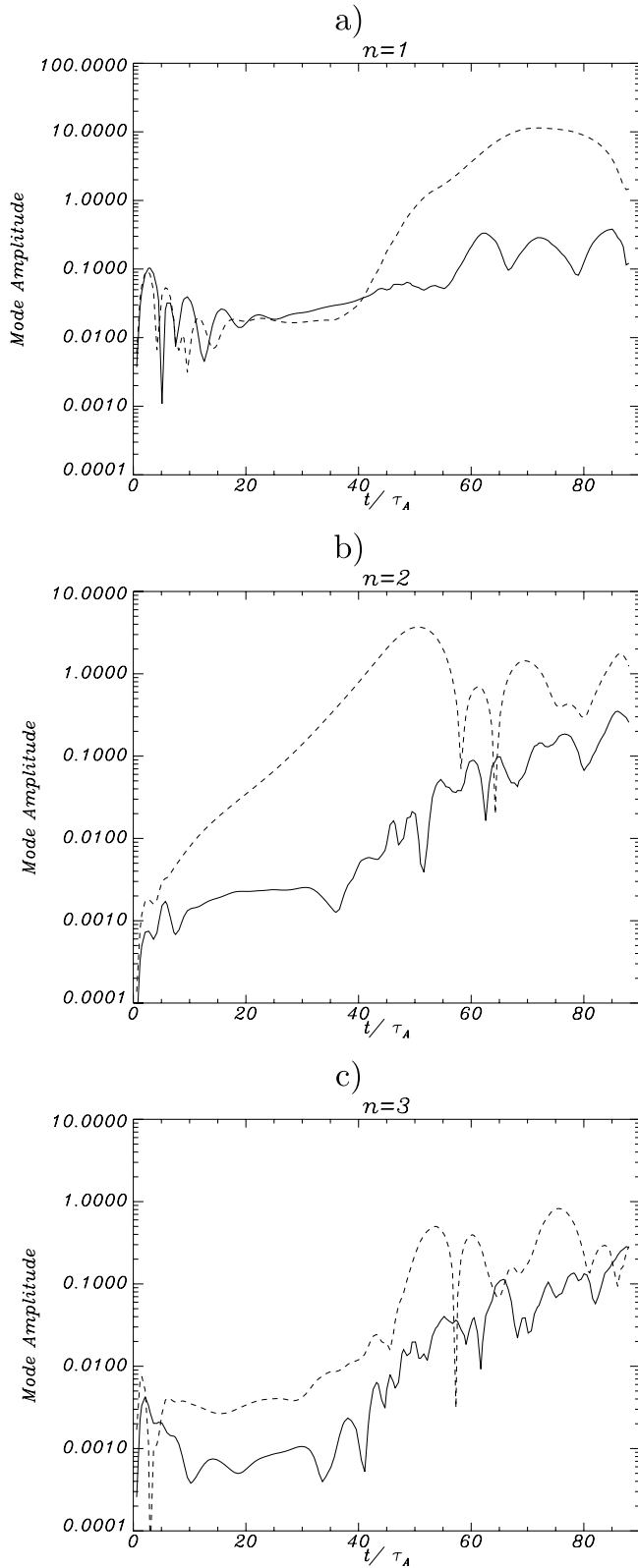


Figure 7. Evolution of the amplitude of the three unstable $m = 1$ (solid) and $m = -1$ (dashed) modes in a periodic system. Run with Spitzer resistivity with reference $S = 10^3$ and uniform viscosity corresponding to $Re = 10^3$.

the discretization. The unstable modes present a clear and extended linear phase followed by a nonlinear coupling of the different Fourier components. The growth rate in the linear phase can be compared with the linear theory.

[46] Table 1 compares linear theory and simulation results for the unstable $m = 1, 2$ modes. Agreement is within the uncertainty of the detection algorithm. The uncertainty is computed by Fourier analyzing different field components for different time intervals and measuring the spread. This uncertainty does not include the contribution of the discretization error, but a convergence study is conducted in time and space demonstrating that the discretization error is lower than the uncertainty in the detection algorithm. For comparison, the same Fourier analysis is repeated for the same case but with Spitzer resistivity (still with $S = 10^3$), and density given by $n = \sqrt{\rho}$, showing similar results and comparable growth rates (see Figure 7).

[47] Besides the growth rate, the eigenfunction of each mode can be compared with the results of the linear theory. Figure 8 shows the three eigenfunctions of the three components of the velocity from linear theory and from the simulation, both with uniform resistivity. The eigenfunctions have the correct parity and the general shape is recovered well in the simulation for all three components. The eigenfunctions are obtained directly from the simulation results at a time when the ($m = 1, n = 1$) mode dominates but are still contaminated by contributions of other modes and in particular by Alfvén waves propagating in the outer regions (shown as wiggles in the velocity field).

4.2. Finite Flux Ropes

[48] When the same case considered above ($B_0 = 1$ with Spitzer resistivity) is repeated using either line-tying at both ends or line-tying at one end and free boundary at the other, the results change very significantly. When nonperiodic boundary conditions are used, the Fourier analysis loses its ability to detect the modes in the system. The eigenfunctions of nonperiodic systems are no longer simple harmonic functions of z and couple different Fourier modes [Einaudi and Van Hoven, 1983; Ryutov et al., 2004]. A better measure of the growth of the kink mode is provided by analyzing the energies: a consequence of the kink instability is the conversion of magnetic energy into kinetic and thermal energy. Overall energy conservation is valid only in the case of periodic systems, while other boundary conditions may allow outflow of energy from the system. In particular, the open boundary case allows energy and momentum to leak out of the open boundary making this case fundamentally different from either line-tied or periodic cases.

[49] The growth of the kinetic energy in the system is shown in Figure 9 for three cases: periodic rope (Figure 9a), rope tied at both ends (Figure 9b), and rope tied at one end and free at the other (Figure 9c). The case considered here is violently unstable in the periodic case, with the kinetic energy increasing from its initial perturbation level (due to the use of a Cartesian grid to represent a cylindrically symmetric state) by two orders of magnitude.

[50] The free-ended case is more unstable and shows a faster initial growth of the kinetic energy. However, the energy in the free-ended case can leave the system from the axial ends and tends to accumulate to a lower level than in

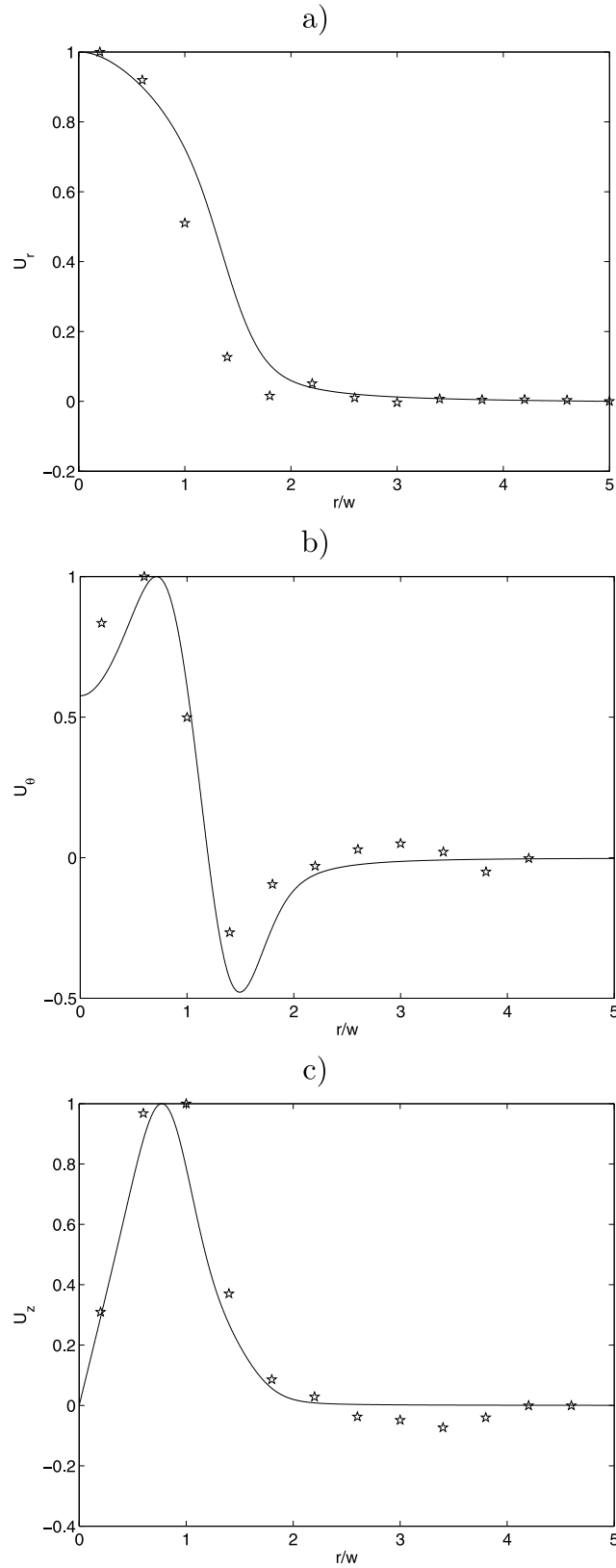


Figure 8. Eigenfunctions for the velocity field of the $m = 1$, $n = 1$ mode. Results from the simulation code are shown as stars, results from linear theory are shown as a solid lines. The ratios between the peak value of each component are: $u_\theta/u_r = 1.74$, $u_z/u_r = 2.64$, from linear theory and $u_\theta/u_r = 1.56$, $u_z/u_r = 2.78$, from the simulation results.

the periodic case. Furthermore, the tied end cannot move, reducing the total displacement possible and further reducing the saturation energy. The line-tied case, instead, is stable even for this relatively strongly unstable case (for periodic ropes).

[51] To confirm the relative stability of the three types of systems, another configuration is chosen. If B_0 is reduced, the safety factor increases to levels where the KS limit is no longer exceeded and the rope remains stable in the periodic case. Figure 10 shows the case with $B_0 = 1/5$ where the minimum value of the safety factor is $q = \pi/2$ largely above the stability limit for periodic systems ($q > 1$) but below the stability limit for free-ended systems ($q < 2$). Clearly, the periodic and line-tied runs remain stable where, instead, the free-ended rope remains violently unstable.

[52] The simulation results above confirm previous experimental and theoretical works [Ryutov *et al.*, 2006; Furno *et al.*, 2006] that suggested that free-ended ropes are more susceptible to the kink instability. It is worth remarking that while previous models were limited to the slender-rope approximation, here the results are computed for a realistic model of flux ropes including Spitzer resistivity, as appropriate for the accurate description of the RSX device.

5. Saturation of the Kink Instability

[53] The case of periodic ropes is considered first, to make a direct link with previous theoretical work, primarily with the theory of the bubble state model by Rosenbluth *et al.* [1976]. The mechanism of saturation of the kink instability in the present circumstances is illustrated in Figure 11–14. The results are for a simulation with periodic boundary conditions, with $B_0 = 1$, $n = \sqrt{p}$ and resistivity given by the Spitzer formula. The figures show a 2-D cross section of a 3-D simulation at four different times during the evolution. The quantities shown are the density ρ , the axial current, the temperature, and the so-called helical flux. In the limit of reduced MHD [Biskamp, 1993], the helical flux is

$$\psi = \psi_p - \frac{n}{m} \frac{B_{0z} \pi r^2}{L} \quad (14)$$

where n and m are the mode numbers and ψ_p is the poloidal flux. Each set of mode quantum numbers leads to a different helical flux. In the present case the most interesting is $m = 2$, $n = 1$, for reasons that will become apparent below. The figures also report two lines: the black line is the intersection of the mode resonant surface $q = 2$ with the plane of the figures, the magenta line is the radius of saturation predicted by the bubble state model by Rosenbluth *et al.* [1976].

[54] The overall evolution entices the progressive displacement of the plasma column (its kink, giving the instability its name) until the surface of the dominant resonant mode is reached. The displacement can be observed for all quantities plotted. In the present case the relevant surface where the displacements stalls turns out to be $q = 2$ (depicted in black, see Figure 13). The fact that the relevant mode resonant surface is $q = 2$ is in itself not a foregone conclusion and it is not related to the linear stability or the fastest growing mode. Below, a model is

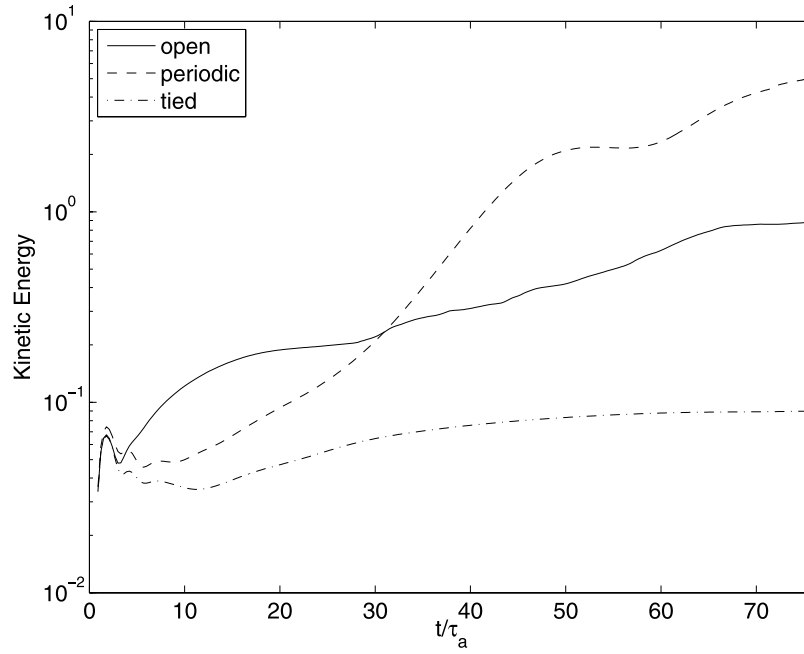


Figure 9. Evolution of the kinetic energy for a flux rope with $B_0 = 1$ for periodic boundary conditions, for line-tying at both ends and for a case with line-tying at one end and open at the other (labeled as open).

provided to explain why that is the important mode resonant surface and to predict it based on an analytical model.

[55] Once the plasma reaches the mode resonant surface, further motion is impeded by the need to pass the resonant surface seen by the plasma as a wall. Until this time, the

evolution of the mode is ideal, but once the resonant surface is reached, nonideal effects become important. At early stages before the plasma reaches the mode resonant surface, helical surfaces can cross the lines because resistivity is high (the temperature is low). However, as the plasma

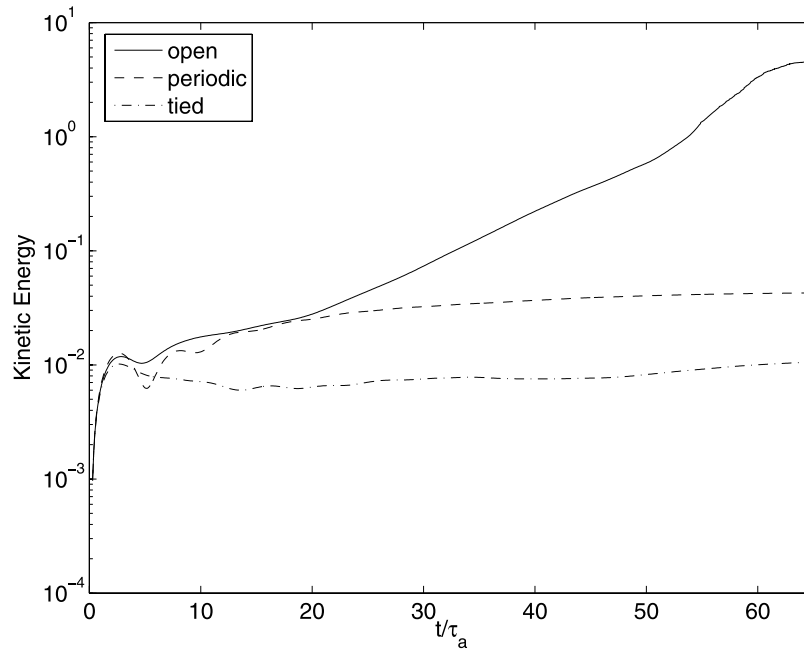


Figure 10. Evolution of the kinetic energy for a flux rope with $B_0 = 1/5$ for periodic boundary conditions, for line-tying at both ends and for a case with line-tying at one end and open at the other (labeled as open).

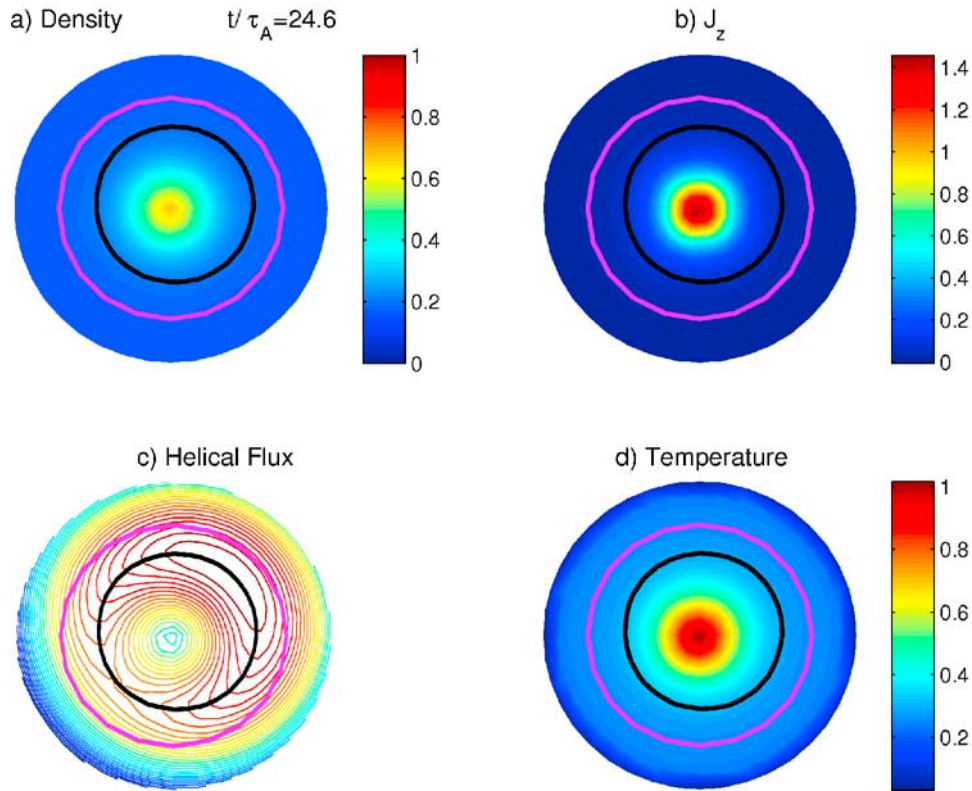


Figure 11. Run with periodic boundary conditions, $B_0 = 1$ at time $t/\tau_A = 24.6$, during the linear phase. False color representation of four significant quantities in two-dimensional (2-D) a section of the 3-D simulation at $z = L_z/2$. Quantities shown: (a) Density, (b) axial current, (c) helical flux (for mode numbers $m = 2$, $n = 1$), (d) temperature. In each panel the thick black line is the intersection of the $q = 2$ surface with the plane of the figure and the magenta line is the line corresponding to the saturation radius predicted by the bubble state theory [Rosenbluth *et al.*, 1976] (see text).

approaches the mode resonant surface, the temperature increases and resistivity drops, slowing the process of flux surfaces crossing the mode resonant surface. Yet the evolution does not stop here. The plasma still evolves more slowly, filling the region circled by the magenta line. To do so, it must cross the mode resonant surface $q = 2$ (black line) at speeds determined by the reconnection process required to cross the surface. Evidence of reconnection is seen in the break up and reconnection of the helical flux surfaces leading to the progressive erosion of the island of initially centrally located helical flux (see Figure 13 and compare with the corresponding figures for previous times, Figures 11–12). By the end time, the island has completely disappeared (see Figure 14). Reconnection is also accompanied by the formation of a ribbon of current [Gerrard and Hood, 2003] evident in Figure 13 as the narrow region of inverted (blue) current near the $q = 2$ surface (black line). The link between inverted currents and reconnection in flux ropes is also supported by experimental evidence [Furno *et al.*, 2005].

[56] Furthermore, the reconnection process is accompanied by heating of the plasma visible in Figure 13 as areas of higher temperature in the regions formed on the separatrix around the magnetic island. Note that Figures 11–14 are 2-D cuts of a 3-D system and island and x-point are to

be regarded as extending out of the plane in a helically symmetric way.

[57] The eventual steady state is characterized by a completely displaced plasma column that has reached the maximum displacement radius (the magenta line). The helical flux no longer presents any remnant of the initially centrally located island but is monotonically decreasing away from its maximum located in proximity of the magenta line. The current and the temperature, instead, remain primarily localized within the dominant resonant surface at $q = 2$.

[58] Note that the region between the dominant mode resonant surface (black line) and the eventual saturation radius (magenta line) does not show any of the traces of reconnection mentioned above: there is no island formation at the saturation radius, there is no heating of the plasma and there is no inverted current forming. The only quantity that clearly shows that the plasma has reached its saturated level is the density. Note in particular how the plasma density tends to spread along the saturation radius. The saturated magenta line is a purely theoretical line based on the theory by Rosenbluth *et al.* [1976] but with no direct physical identity, yet the plasma density runs against it and spreads along it as if it was water flowing against a physical wall. This is a remarkable indication that the saturation line is

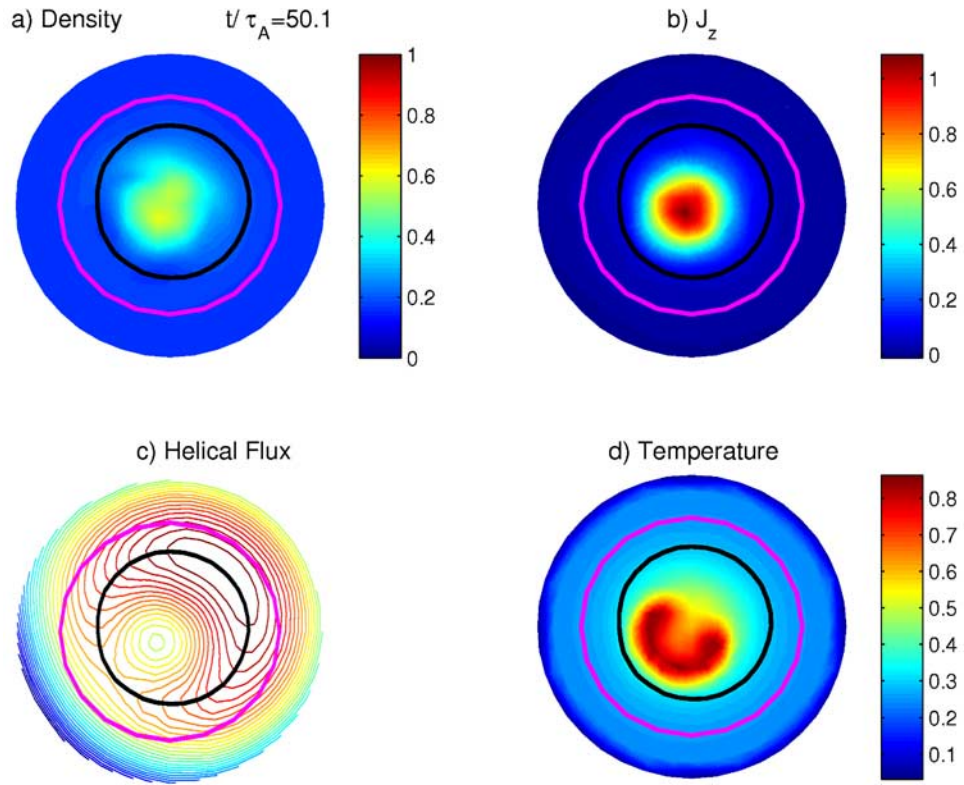


Figure 12. Run with periodic boundary conditions, same as Figure 11 but at time $t/\tau_A = 50.1$, near the end of the linear phase.

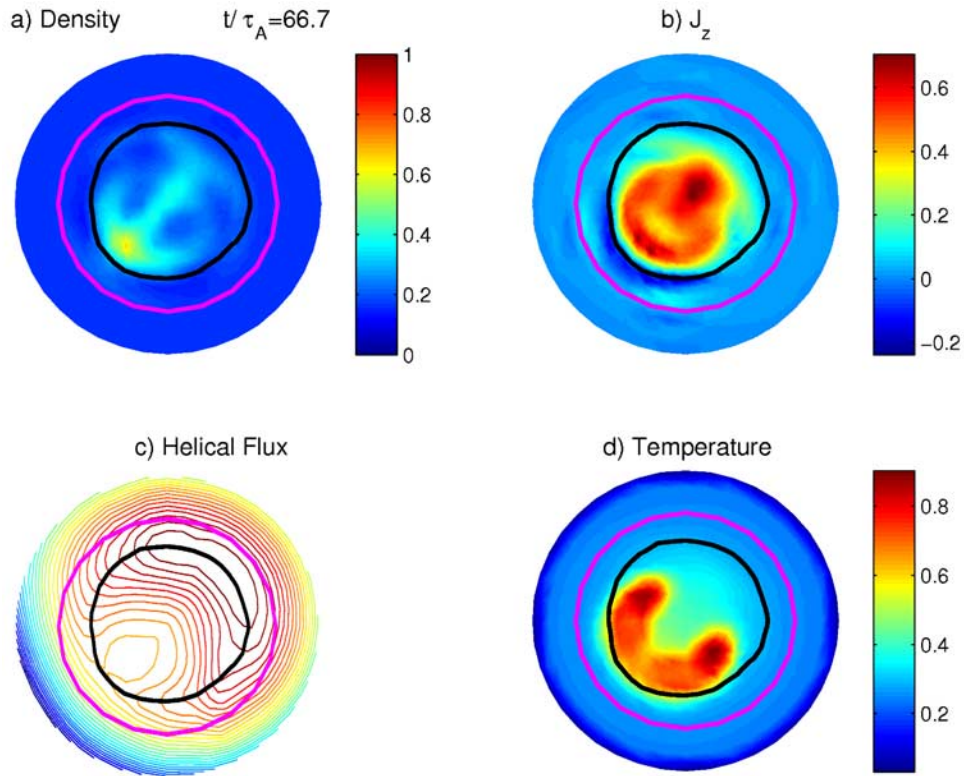


Figure 13. Run with periodic boundary conditions, same as Figure 11 but at time $t/\tau_A = 66.7$, during the first nonlinear phase, where the plasma column reconnects and passes through the mode resonant surface $q = 2$ (black line).

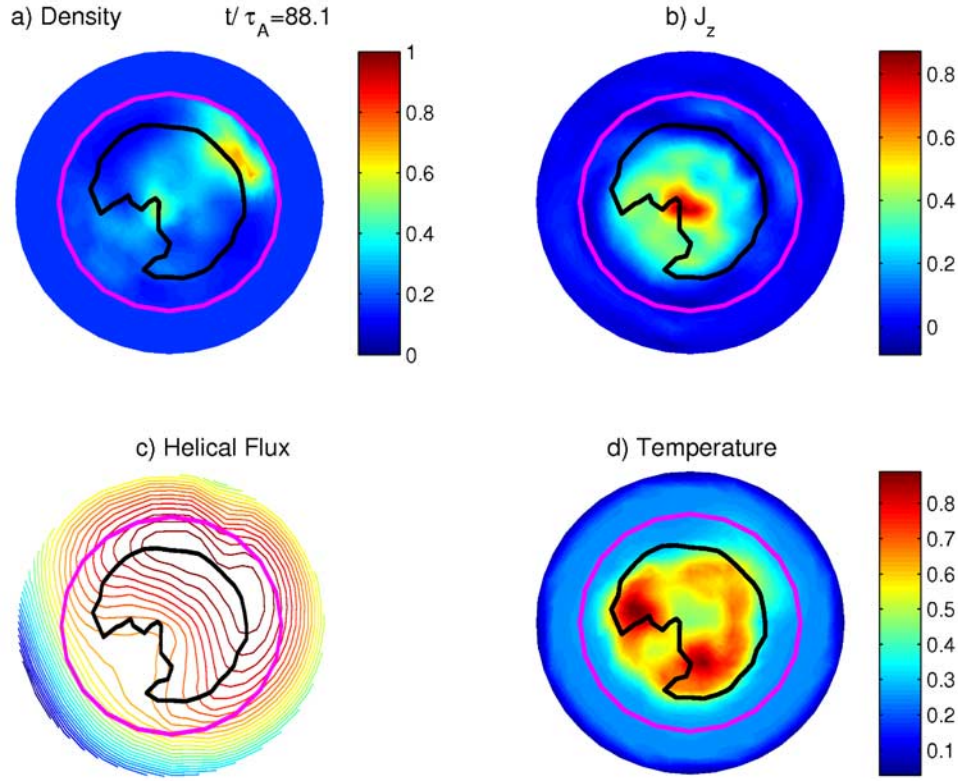


Figure 14. Run with periodic boundary conditions, same as Figure 11 but at time $t/\tau_A = 88.1$ corresponding to the saturated state.

really predicted correctly by the theory due to *Rosenbluth et al.* [1976] and summarized below.

5.1. Bubble State Model of the Saturation Mechanism

[59] The overall phenomenological description above can be made quantitative by introducing a mathematical model based on the so-called reduced MHD picture (also known as Strauss model in America and Kadomtsev-Pogutse in the former Soviet Union) [*Kadomtsev and Pogutse*, 1973; *Strauss*, 1976; *Kadomtsev*, 1992]. The model predicts what is the dominant resonant mode (and correspondingly what is the mode resonant surface, black line) and what is the eventual saturation circle (magenta curve). Below, the model is summarized and its results are compared quantitatively with the simulation results.

[60] The reduced MHD model can be based on the assumption that the plasma is immersed in a large external field. In the present work the rope is produced in a vacuum chamber with a strong uniform axial field $\mathbf{B}_0 = B_z \hat{\mathbf{z}}$.

[61] The magnetic field and velocity field are both assumed to be divergence free (obvious for \mathbf{B} , but an approximation for \mathbf{v}):

$$\mathbf{B} = B_z \hat{\mathbf{z}} + \hat{\mathbf{z}} \times \nabla_{\perp} \psi_p \quad (15)$$

$$\mathbf{v} = v_z \hat{\mathbf{z}} + \hat{\mathbf{z}} \times \nabla_{\perp} \phi \quad (16)$$

where $\hat{\mathbf{z}}$ is the unit vector in the z direction and ∇_{\perp} is the gradient operator in the plane normal to z , in cylindrical coordinates: $\nabla_{\perp} = \hat{\mathbf{r}} \partial_r + (\hat{\boldsymbol{\theta}}/r) \partial_{\theta}$. The new functions are

called poloidal flux function ψ_p and stream function ϕ , respectively.

[62] The equations for reduced MHD follow from an asymptotic expansion in the inverse aspect ratio $\epsilon = w/L_z$. The ensuing equations are [*Biskamp*, 1993]

$$\begin{aligned} \rho \left(\frac{\partial \xi}{\partial t} + \mathbf{v}_{\perp} \cdot \nabla_{\perp} \xi \right) &= \mathbf{B} \cdot \nabla j_z + \mu \rho \nabla^2 \xi \\ \frac{\partial \psi_p}{\partial t} + \mathbf{v}_{\perp} \cdot \nabla_{\perp} \psi_p &= B_z \frac{\partial \phi}{\partial z} + \eta \nabla^2 \psi_p \end{aligned} \quad (17)$$

where dimensionless quantities (as described in section 3) are used. The axial current is computed from

$$j_z = \nabla_{\perp}^2 \psi_p \quad (18)$$

and the axial component of the vorticity is computed as

$$\xi = \nabla_{\perp}^2 \phi \quad (19)$$

Note that the axial velocity v_z is decoupled from the other equations and need not be assumed constant or zero. However, for the present purposes it can be neglected [*White*, 2001].

[63] A crucial property of the reduced MHD equations (17) is that of admitting an energy integral of motion. For the purpose of deriving a simplified model for the saturation of the external kink mode observed in the simulations, a simplified configuration is considered of a simply connected

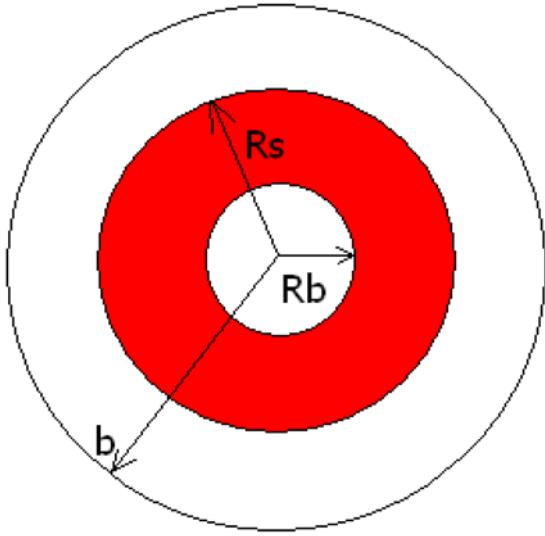


Figure 15. Schematic representation of a bubble state.

plasma region surrounded by vacuum and further surrounded by a circular wall. Moreover, a single helicity mode is assumed where all quantities depend on the axial and angular direction harmonically, e.g.,

$$\psi_p(r, \theta, z, t) = \psi_p(r, t)e^{-i2\pi n z/L_z - im\theta} \quad (20)$$

where the same symbol is used for the whole quantity and its harmonic component.

[64] Under these circumstances an energy integral can be derived by multiplying scalarly the first of equation (17) with \mathbf{v}_\perp :

$$E_b = \frac{1}{2} \int_{pla} [\rho(\nabla\phi)^2 + (\nabla\psi)^2] dV - \frac{1}{2} \int_{vac} (\nabla\psi)^2 + 2\pi\psi_w \quad (21)$$

where the helical flux ψ has been used. The first integral is computed within the plasma region and the second within the vacuum region. The integral above is a constant of motion under the hypothesis that the helical flux at the wall, ψ_w , is held constant, as appropriate for an ideal wall.

[65] The configuration under investigation does not exactly fit this model. The plasma density and current falls off rapidly from the center, but it is not quite a sharp transition between vacuum and plasma. The choice of a continuous profile in the simulations is dictated by the need to represent the plasma in RSX with fidelity. Nevertheless, the initial configuration can be represented reasonably well by a plasma column of radius approximately $a = w$ carrying the whole current in the system, surrounded by vacuum and by a wall at radius $b = 5$. The model is accurate in two ways. First, the total current is a crucial parameter for the kink instability and is preserved. Second, the outer region in the simulations and in RSX is not quite vacuum but it has the main property of vacuum from the perspective of studying the kink instability; it has a very large resistivity (thanks to a lower temperature and the use of Spitzer resistivity). This latter point is what characterizes the present configuration as an external kink mode rather than

an internal kink mode where magnetic field surfaces mix and reconnect within the plasma.

[66] On the basis of these approximations, the integral of motion E_b can be used [Rosenbluth *et al.*, 1976] to determine the lowest energy state and to pose the question if that is indeed the relaxed state of the plasma column after saturation of the kink mode. To analyze this point, the concept of “bubble state” is introduced. A bubble state is defined as a state where a (uniform in density and current) plasma is displaced radially to form a shell (of inner radius r_b and outer radius $r_s = \sqrt{r_b^2 + a^2}$) circling a vacuum bubble and further surrounded by more vacuum and eventually by the wall. Figure 15 shows the concept. Note that the configuration of a bubble state is a single helicity state, with a specific m and n . The radial dependence shown in Figure 15 is further modulated by the angular harmonic dependence with mode number m and axial dependence with mode number n .

[67] The integral E_b can be computed analytically in this case and the resulting energy is

$$E_b = \pi \frac{r_s^2 a^2}{2} - \frac{\pi}{\ln(r_s/b)} \left(\frac{b^2 - r_s^2}{2} + \psi_w \right)^2 \quad (22)$$

where $\psi_w = n(a^2 - b^2)/m - (a^2/q_a)\ln(a/b)$. The plasma is assumed to have a uniform current and its safety factor is correspondingly uniform (within the plasma) and equal to q_a .

[68] Equation (22) provides a theoretical prediction of what is the dominant mode and the radius of saturation for the kinked rope. The equilibrium relaxed state is predicted to be the bubble state of minimum energy. Depending on the plasma radius, a , the wall radius, b , the plasma safety factor q_a , and the ratio of the quantum numbers m/n of a kink mode, the energy E_b of a bubble state of radius r_s can be lower or higher than the unperturbed state given by the rope remaining on axis. Note that the existence of a bubble state of energy lower than the unperturbed state is not logically directly linked to the stability of a rope. The stability or instability implied by the nonexistence or existence of a lower-energy bubble state is a nonlinear stability concept, not directly linked to linear stability.

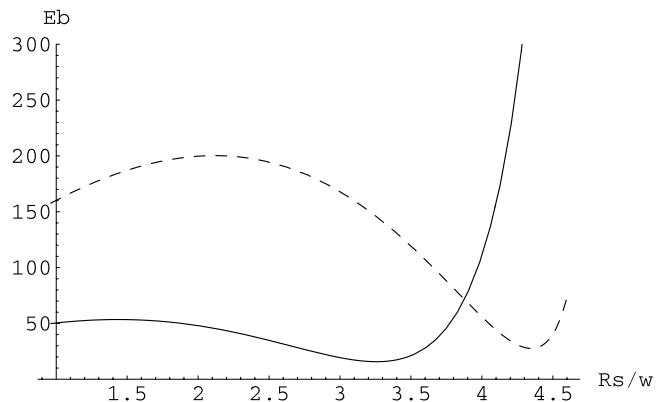


Figure 16. Energy of the bubble state for different outer radii R_s . Mode $m/n = 2$ is shown as a solid line, mode $m/n = 3$ is shown as a dashed line.

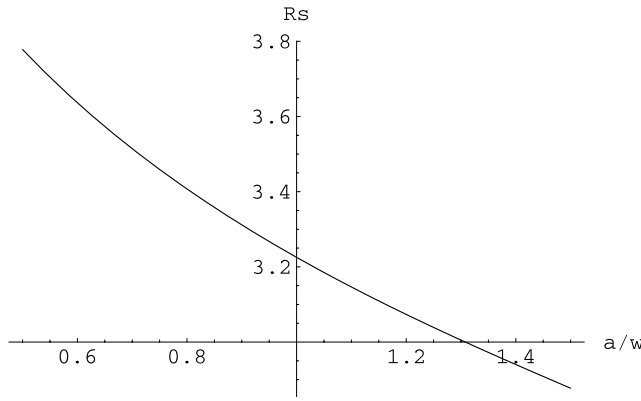


Figure 17. Dependence of the radius of the minimum energy bubble state for mode $m/n = 2$ as a function of the plasma radius a .

5.2. Comparison of the Bubble State Model With Simulation Results

[69] For the case under consideration ($B_0 = 1$), the model described above is analyzed assuming $a = w = 1$ and $b/w = 5$, with a uniform current inside the plasma equal to the total current in the simulation. Figure 16 shows the energy of modes $m/n = 2$ and $m/n = 3$. All other modes do not present a lower energy bubble state. Note that the bubble state with $m/n = 2$ has a slightly lower energy than modes $m/n = 3$. Note also that the minimum energy for modes $m/n = 3$ is so close to the wall to interfere with the immersed boundary method description of the wall, which becomes a cell-wide transition region, reaching $r = 4.6$.

[70] On the basis of the model of bubble states, the prediction is that the plasma column should reach a relaxed state at $r_s/w = 3.23$ and that at saturation mode number $m = 2$, $n = 1$ should dominate. Note that the prediction is based on the somewhat arbitrary decision to consider the position of the plasma/vacuum interface in the initial state equal to w . Figure 17 investigates the sensitivity of the prediction to this choice. As can be observed, even a drastic change in the plasma radius used for the bubble state calculation only changes the radius of relaxation by small values.

[71] Figure 14 shows the final relaxed state and depicts (in magenta) the radius corresponding to the predicted relaxation radius $r_s/w = 3.23$. The agreement is remarkable. Furthermore, as noted above, in the intermediate phase of relaxation when the plasma surpasses the mode resonant surface, it is the surface corresponding to $q = m/n = 2$ that is relevant, confirming that the dominant mode for the nonlinear relaxation is indeed mode ($m = 2$, $n = 1$).

[72] Finally, yet another confirmation that the dominant mode for saturation is the $m = 2$, $n = 1$ mode can be obtained by observing the spectrum at saturation, shown in Figure 18. In each figure, the contribution of positive and negative m modes is summed, and the spectrum is represented as a function of the quantum number n . Symmetry with n correctly descends from the definition used. Note that a large number of modes coexist, but the mode $m = 2$, $n = 1$ is dominant as predicted by the theory described above.

[73] The bubble state model is based on the reduced MHD description of a single helicity state. The reality in the simulation is remarkably different. Figure 18 shows that besides the main mode, many others are present. Indeed the final state is not simply a $m = 2$ mode. It shows an elliptical shape of the deformed column (a property of the $m = 2$ mode) but also a net displacement off center (a property of the $m = 1$ mode). Yet it is remarkable that this mixed helicity final state still remains confined within the circle predicted by the single helicity bubble state.

[74] As noted in the summary of the derivation above, the bubble state theory by *Rosenbluth et al.* [1976] deals with nonlinear considerations unrelated to linear stability. Indeed, when the bubble state theory is applied to the stable case with $B_0 = 1/5$ (see Figure 10), the bubble state theory predicts a nonlinear more stable bubble state with a displacement $r_s/w = 3.84$ (with mode number $m/n = 4$) larger than in the linearly unstable case $B_0 = 1$. This conclusion is indirectly confirmed by the comparison of the saturation

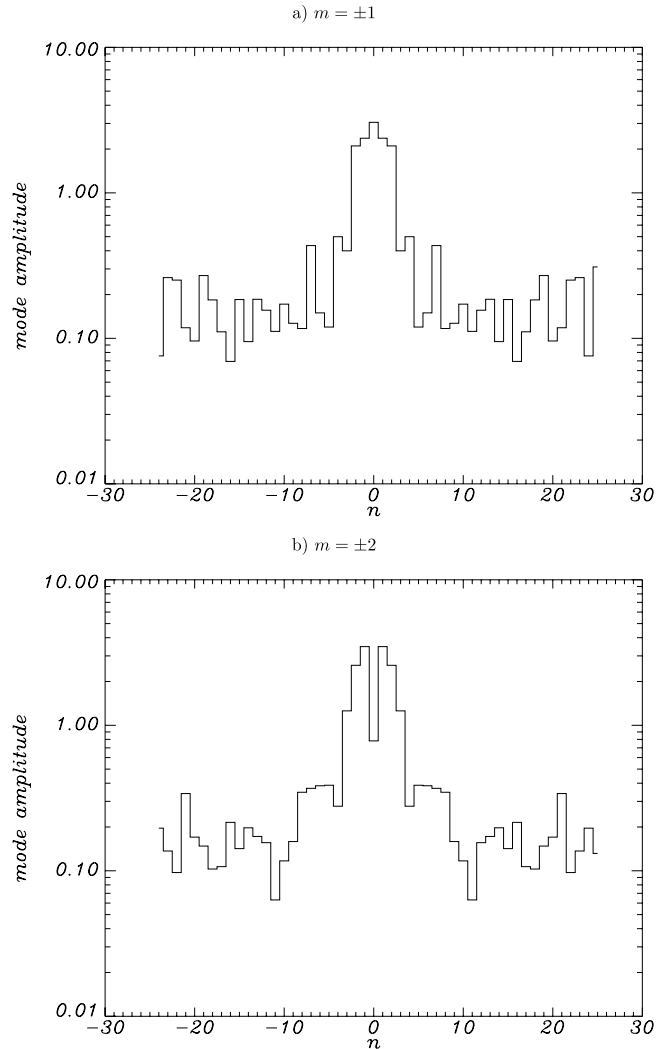


Figure 18. Periodic system with $B_0 = 1$. Spectrum at saturation ($t/\tau_A = 87$), for mode numbers $m = \pm 1$ (a) and $m = \pm 2$ (b) as a function of n .

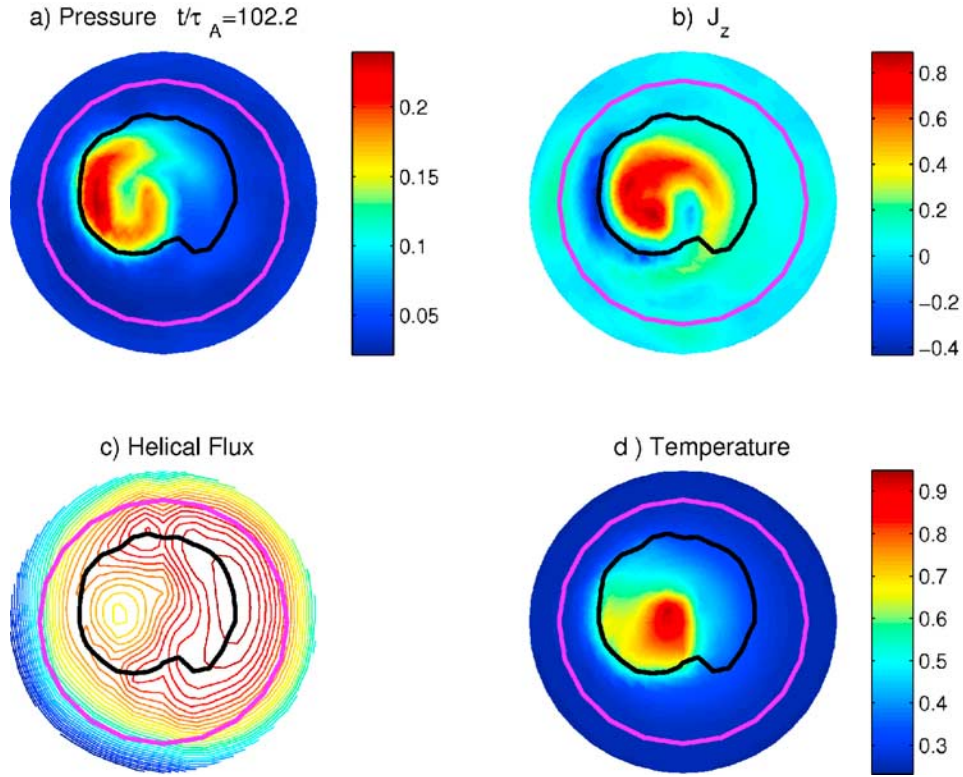


Figure 19. Run with free/line-tied boundary conditions, $B_0 = 1$. False color representation of four significant quantities near the end of the linear phase in 2-D a section of the 3-D simulation at $z = L_z$: (a) Density, (b) axial current, (c) helical flux (for mode numbers $m = 2, n = 1$), (d) temperature. The black and magenta line have the same meaning as in Figure 11.

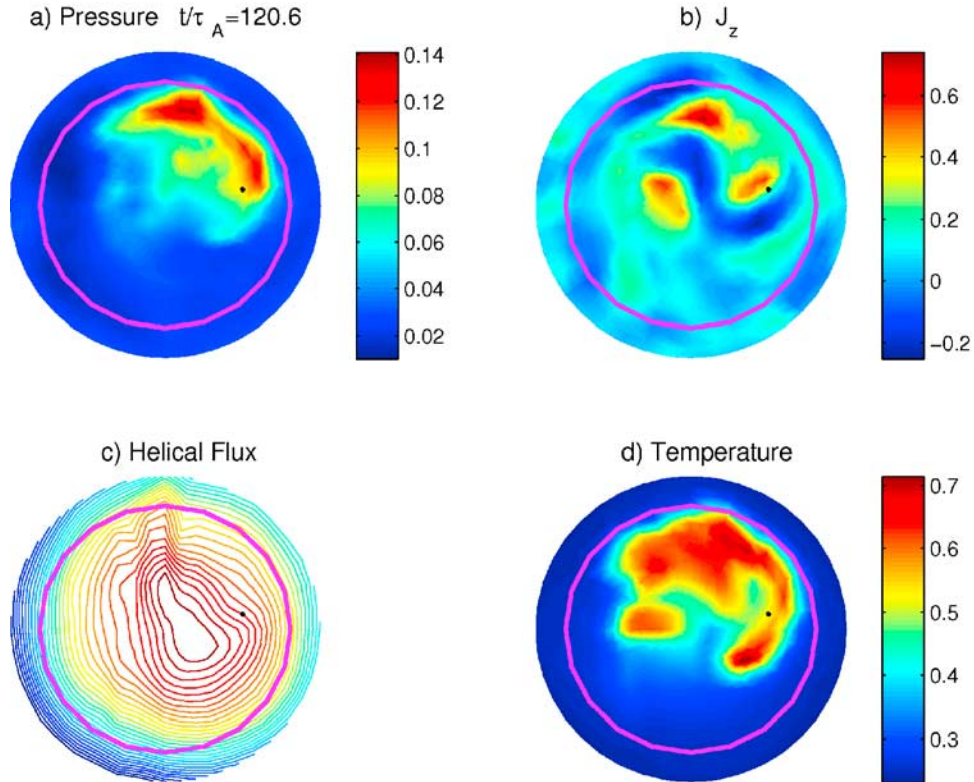


Figure 20. Run with free/line-tied boundary conditions, same as Figure 19 but at time $t/\tau_A = 120.6$.

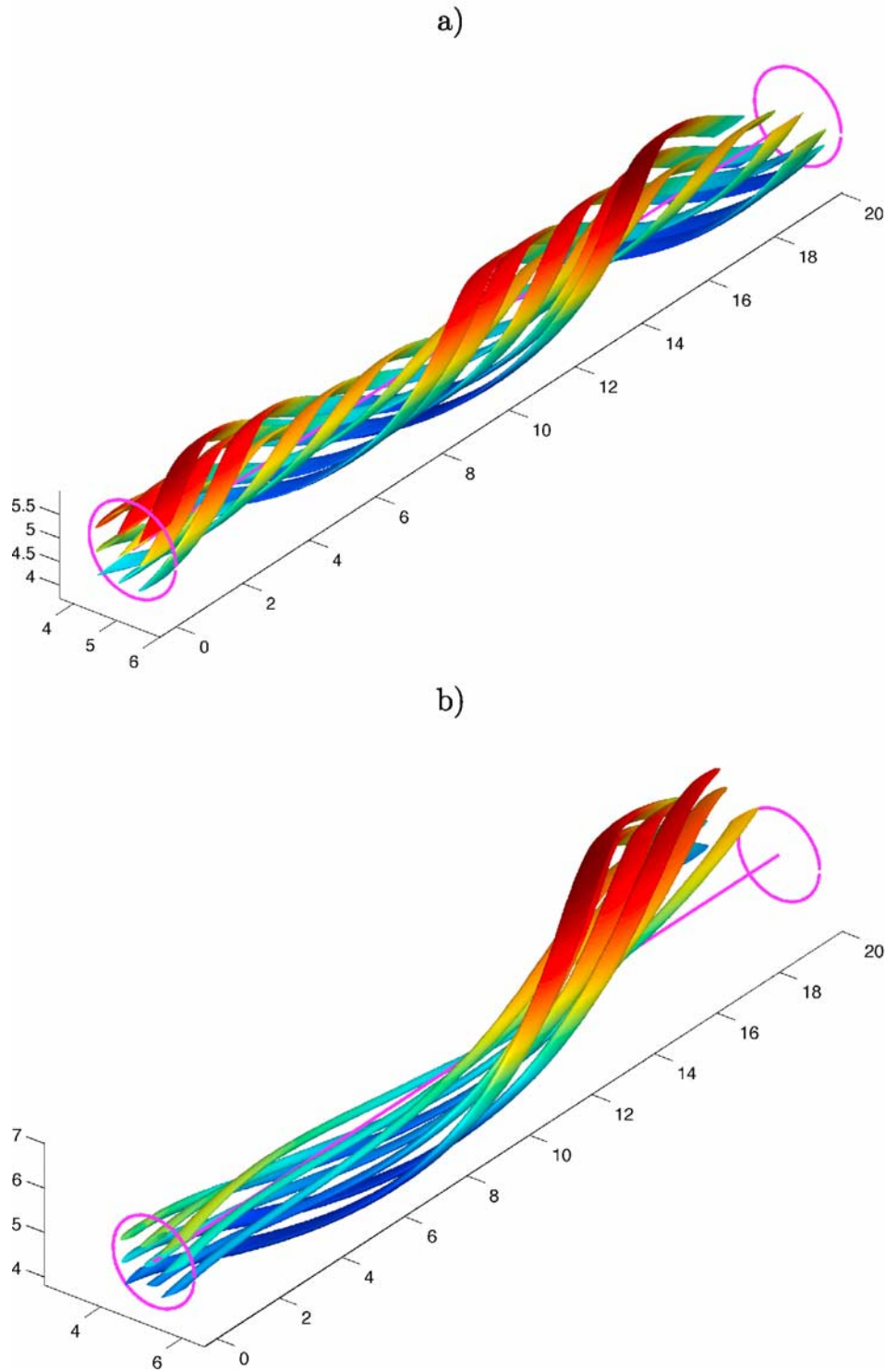


Figure 21. Magnetic flux tubes within a rope tied at one end and free at the other. Two times are shown: initial state (a) and at saturation, $t/\tau_A = 120.6$. (b) The color shows the height along the z axis.

level for the kinetic energy as shown in Figures 9–10 for the free-ended ropes where both cases are linearly unstable. The saturation level for the more linearly unstable case $B_0 = 1$ is lower than that for $B_0 = 1/5$, in accord with the bubble state prediction (even though the bubble state prediction

applies strictly only to the periodic case). This result, however, is only suggestive as it might also be affected by the indirect relationship between the displacement and the saturation level of the kinetic energy, affected also by the

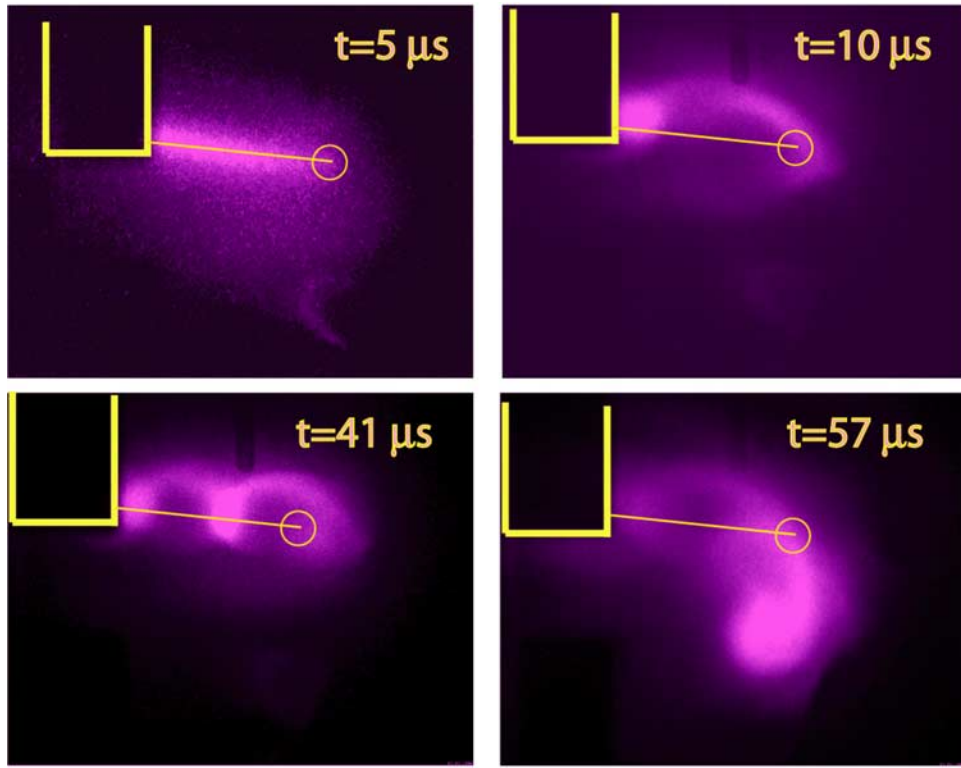


Figure 22. Sequence of images taken from a camera with a oblique view angle along the axial direction (see Figure 4). Four subsequent times are shown illustrating the progressive kink and its saturation to a state line-tied at the plasma gun but free at the free end. The largest displacement is at the free end.

outflow of energy from the open boundary of the simulation box.

6. Saturated State of a Free/Tied Flux Rope

[75] The analysis reported above is valid for a periodic system, and the study of the bubble states assumes the existence of modes with defined helicity in a periodic system. For the case with line-tying at one end and free boundary conditions at the other, the analysis cannot be applied directly.

[76] However, Figures 19–20 show the configuration of a free-ended rope for the same parameters considered in the previous section ($B_0 = 1$, Spitzer resistivity with $S = 10^3$). As can be observed the intermediate nonlinear phase is still dominated by the surface $q = 2$. Furthermore, the final relaxed state is still determined by $r_s/w = 3.23$ as in the periodic case.

[77] There is, however, a fundamental difference. Figures 19–20 show a cross section of the plasma rope at $z = L_z$. Closer to the line-tied end, the rope is less displaced up to no displacement at all at the tied end. Figure 21 shows a 3-D representation of the flux rope in its initial configuration and its relaxed state. Note how the line-tied end (closer to the reader) remains fixed, while the free end moves away. A circle in pink is shown for reference to remind of the initial position of the rope.

[78] The simulations shown here are but a qualitative representation of the real system in RSX. Future experi-

mental work will have to test the observations made in the simulations regarding the saturation level and the properties of the saturated state. The experiments available thus far provide already a confirmation to one of the conclusions described above regarding the saturated state of a rope free at one end and tied at the other. Figure 22 shows four subsequent figures taken from the camera angle along the plasma rope shown in Figure 4. The subsequent shots provide evidence of the increasing kinking of the initially straight rope. The final state is clearly still tied to the plasma gun generating the rope and is progressively more displaced, spiraling outward as observed in the simulations. Future work will be needed to make a quantitative connection between the relaxed maximum displacement observed in the simulations, predicted by the bubble state model of *Rosenbluth et al.* [1976] and experiments.

7. Conclusions

[79] The results above can be summarized into two findings. First, the ranking of ropes according to their liability to the kink instability is free-ended flux ropes are the most unstable, with their stability needing $q > 2$, periodic ropes come next, with the classic KS limit to determine their stability. The most stable are line-tied flux ropes. This finding is of significance to solar and astrophysical flux ropes where the case of free-ended ropes may be relevant and their reduced stability limit needs to be taken into account.

[80] Second, the mechanism for nonlinear evolution progresses in two steps. The first onsets when the plasma column reaches the dominant mode resonant surface. Here, reconnection is needed for the plasma to progress further. The actual rate of reconnection is beyond the scope of the present paper. Spitzer resistivity is used within the regular resistive model; in real systems the situation is more complicated because of the presence of other nonideal mechanisms besides just collisional resistivity. The last stage of the evolution is the formation of a bubble state where the plasma reaches the radius predicted by a simple model due to *Rosenbluth et al.* [1976]. A significant distinction needs to be made between the tied/free-ended and the periodic case. The tied end has zero displacement at saturation, while the displacement spirals out away from the tied end. The maximum displacement is at the free end and it is the same as in the periodic case.

[81] The conclusions reached above can be compared with experiments conducted on RSX. The decreased stability of free flux ropes has indeed been observed in experiments [*Furno et al.*, 2006]. The typical saturated column has the spiral structure observed here [*Furno et al.*, 2006, 2005]. The key prediction above about the ability of the bubble-state mode to predict the saturation level needs yet to be investigated experimentally.

[82] **Acknowledgments.** The authors gratefully acknowledge useful discussions with Amitava Bhattacharjee, Daniele Bonfiglio, Susanna Cappelletti, Dominique Escande, John Finn, Roberto Lionello, Dimitri Ryutov, and Dalton Schnack. This research is supported by the LDRD program at the Los Alamos National Laboratory and by the Office of Fusion Energy Science at the Office of Science of the United States Department of Energy. Work conducted under the auspices of the United States Department of Energy contract W-7405-ENG-36.

[83] Amitava Bhattacharjee thanks the reviewers for their assistance in evaluating this paper.

References

- Baty, H., G. Einaudi, R. Lionello, and M. Velli (1998), Ideal kink instabilities in line-tied coronal loops, *Astron. Astrophys.*, **333**, 313.
- Biskamp, D. (1993), *Nonlinear Magnetohydrodynamics*, Cambridge Univ. Press, New York.
- Blandford, R. (2002), Blood out of a stone, *Science*, **295**, 1653.
- Brackbill, J. (1991), FLIP MHD: A particle-in-cell method for magnetohydrodynamics, *J. Comput. Phys.*, **96**, 163.
- Brackbill, J., and D. Knoll (2001), Transient magnetic reconnection and unstable shear layers, *Phys. Rev. Lett.*, **86**, 2329–2332.
- Einaudi, G., and G. Van Hoven (1983), The stability of coronal loops: Finite-length and pressure-profile limits, *Sol. Phys.*, **88**, 163.
- Evstatiev, E., G. Delzanno, and J. Finn (2006), A new method for analyzing line-tied kink modes in cylindrical geometry, *Phys. Plasmas*, **13**, 072, 902.
- Fiksel, G., A. Almagri, D. Craig, M. Iida, S. Prager, and J. Sarff (1996), High current plasma electron emitter, *Plasma Sources Sci. Technol.*, **5**, 78–83.
- Freidberg, J. (1987), *Ideal Magnetohydrodynamics*, Springer, New York.
- Furno, I., et al. (2003), Reconnection scaling experiment: A new device for three-dimensional magnetic reconnection studies, *Rev. Sci. Instrum.*, **74**(4), 2324.
- Furno, I., T. P. Intrator, E. W. Hemsing, S. C. Hsu, P. Ricci, and G. Lapenta (2005), Coalescence of two magnetic flux ropes via collisional magnetic reconnection, *Phys. Plasmas*, **12**(5), 055, 702.
- Furno, I., T. Intrator, D. Ryutov, S. Abbate, T. Madziwa-Nussinov, A. Light, L. Dorf, and G. Lapenta (2006), Current driven rotating kink mode in a plasma column with a non-line-tied free end, *Phys. Rev. Lett.*, **97**, 015,002.
- Gekelman, W., J. E. Maggs, and H. Pfister (1992), Experiments on the interaction of current channels in a laboratory plasma: Relaxation to the force-free state, *IEEE Trans. Plasma Sci.*, **20**(6), 614.
- Gerrard, C., and A. Hood (2003), Kink unstable coronal loops: Current sheets, current saturation and magnetic reconnection, *Sol. Phys.*, **214**, 151.
- Goedbloed, H., and S. Poedts (2004), *Principles of Magnetohydrodynamics*, Cambridge Univ. Press, New York.
- Hansen, J. F., S. K. P. Tripathi, and P. M. Bellan (2004), Co- and counter-helicity interaction between two adjacent laboratory prominences, *Phys. Plasmas*, **11**(6), 3177.
- Hood, A., and E. Priest (1979), Kink instability of solar coronal loops as the cause of solar flares, *Sol. Phys.*, **64**, 303.
- Hood, A., and E. Priest (1981), Critical conditions for magnetic instabilities in forcefree coronal loops, *Geophys. Astrophys. Fluid Dyn.*, **17**, 297.
- Kadomtsev, B. (1992), *Tokamak Plasma: A Complex Physical System*, Inst. of Phys. Publ., Philadelphia, Pa.
- Kadomtsev, B., and O. Pogutse (1973), Nonlinear helical plasma perturbations in the tokamak, *Sov. Phys. JETP*, **38**, 283.
- Lapenta, G. (1999), Simulation of charging and shielding of dust particles in drifting plasmas, *Phys. Plasmas*, **6**, 1442.
- Lapenta, G. (2002), Particle rezoning for multidimensional kinetic particle-in-cell simulations, *J. Comput. Phys.*, **181**, 317.
- Lapenta, G., and J. Brackbill (1996), Immersed boundary method for plasma simulation in complex geometries, *IEEE Trans. Plasma Sci.*, **24**, 105.
- Lapenta, G., and D. Knoll (2004), Reconnection in the solar corona: Role of the kink-helmholtz instability, *Solar Phys.*, **214**, 107.
- Lapenta, G., and D. Knoll (2005), Effect of a converging flow at the streamer cusp on the genesis of the slow solar wind, *Astrophys. J.*, **624**, 1049–1056.
- Lapenta, G., and P. Kronberg (2005), Simulation of astrophysical jets: Collimation and expansion into radio lobes, *Astrophys. J.*, **625**, 37–50.
- Lapenta, G., F. Iinoia, and J. Brackbill (1995), Particle-in-cell simulation of glow discharges in complex geometries, *IEEE Trans. Plasma Sci.*, **23**, 769.
- Lionello, R., D. Schnack, G. Einaudi, and M. Velli (1998a), Current sheet formation due to nonlinear kink modes in periodic and line-tied configurations, *Phys. Plasmas*, **5**, 3722.
- Lionello, R., M. Velli, G. Einaudi, and Z. Mikić (1998b), Nonlinear magnetohydrodynamic evolution of line-tied coronal loops, *Astrophys. J.*, **494**, 840.
- Monaghan, J. J. (1992), Smoothed particle hydrodynamics, *Annu. Rev. Astron. Astrophys.*, **30**, 543.
- Owen, F., P. Hardee, and T. Cornwell (1989), High-resolution high dynamic range VLA images of the M87 jet at 2 centimeters, *Astrophys. J.*, **340**, 698.
- Peskin, C. (2002), The immersed boundary method, *Acta Numer.*, **11**, 479.
- Priest, E., and T. Forbes (2000), *Magnetic Reconnection: MHD Theory and Applications*, Cambridge Univ. Press, New York.
- Rosenbluth, M., D. Monticello, H. Strauss, and R. White (1976), Numerical studies of nonlinear evolution of kink modes in tokamaks, *Phys. Fluids*, **19**, 1987.
- Ryutov, D. D., R. H. Cohen, and L. D. Pearlstein (2004), Stability of a finite-length screw pinch revisited, *Phys. Plasmas*, **11**, 4740.
- Ryutov, D. D., I. Furno, T. P. Intrator, S. Abbate, and T. Madziwa-Nussinov (2006), Phenomenological theory of the kink instability in a slender plasma column, *Phys. Plasmas*, **13**, 032, 105.
- Schrijver, C., et al. (1999), A new view of the solar outer atmosphere by the transition region and coronal explorer, *Solar Phys.*, **187**, 261.
- Spitzer, L. (1956), *Physics of Fully Ionized Gases*, Wiley-Interscience, Hoboken, N. J.
- Strauss, H. (1976), Non-linear three dimensional dynamics of noncircular tokamaks, *Phys. Fluids*, **19**, 134.
- Trintchouk, F., M. Yamada, H. Ji, R. M. Kulsrud, and T. A. Carter (2003), Measurement of the transverse Spitzer resistivity during collisional magnetic reconnection, *Phys. Plasmas*, **10**, 319.
- Wesson, J. (2004), *Tokamak*, Oxford Univ. Press, New York.
- White, R. (2001), *The Theory of Toroidally Confined Plasmas*, Imperial Coll. Press, London.
- Zwingmann, W. (1987), Theoretical study of onset conditions for solar eruptive processes, *Solar Phys.*, **111**, 309.

G. L. Delzanno and T. Intrator, Los Alamos National Laboratory, Los Alamos, NM 87545, USA.

I. Furno, Ecole Polytechnique Federale de Lausanne (EPFL), Centre de Recherches en Physique des Plasmas, Association EURATOM-Confederation Suisse, CH-1015 Lausanne, Switzerland.

G. Lapenta, Centre for Plasma Astrophysics, Departement Wiskunde, Katholieke Universiteit Leuven, Celestijnenlaan 200B, BE-3001 Heverlee, Belgium. (giovanni.lapenta@wis.kuleuven.be)